Earth and Planetary Science Letters 542 (2020) 116316

Contents lists available at ScienceDirect

Earth and Planetary Science Letters

www.elsevier.com/locate/epsl

Variation of the equatorial moments of inertia associated with a 6-year westward rotary motion in the Earth

B.F. Chao [a,*], Y. Yu [a,b]

[a] Institute of Earth Sciences, Academia Sinica, Taipei, Taiwan, ROC
[b] Scripps Institution of Oceanography, University of California at San Diego, La Jolla, CA, USA

ARTICLE INFO

Article history:
Received 26 June 2019
Received in revised form 23 December 2019
Accepted 28 April 2020
Available online xxxx
Editor: B. Buffett

Keywords:
rotary motion
6-years
equatorial moments of inertia
gravity field

ABSTRACT

The westward-propagating rotary wave-2 displacement field in the mantle with the period of 6 years (Ding and Chao, 2018) predicts an ensuing 6-year variation in the Earth's two equatorial principle moments of inertia. In this paper we search for such signals in the sectoral Stokes coefficients C_{22} and S_{22} of the Earth's gravitational field. We analyze the monthly ΔC_{22} and ΔS_{22} data series derived from the satellite laser-ranging measurements for 1992-2018 (and the shorter series from the GRACE satellite, 2002-2017). We report unequivocal evidences found in ΔC_{22} and ΔS_{22} that conform to the predicted scenario in both amplitude and relative phasing. Conversely, this further corroborates the 6-year westward wave-2 motion in the Earth.

1. Introduction

A 6-year (or 5.9-year to be more precise) westward-propagating rotary wave-2 motion (a wave with azimuthal wavenumber 2) was observed in the Earth's surface deformation field and geomagnetic field (Ding and Chao, 2018). This wave-2 motion consists of a diagonal double-peak pattern making a westward half-round in 6 years around the globe along the equatorial plane, kinematically analogous to a westward-propagating semi-diurnal tide wave except the period is 6 years rather than ~12 hours. The equatorial double peak is in the form of spatial sectoral spherical harmonic of degree 2 and order 2 (henceforth abbreviated as [2, 2]). Ding and Chao (2018) proposed a causal connection of this wave-2 motion with the inner-core axial torsional libration (ATL) associated in turn with the 6-year oscillation that is observed in the Earth's length-of-day (Chao, 2017, and references therein). The proposed cause of the ATL is the mantle-inner core gravitational (MICG) restoring torque dictated by the product of the two [2, 2] density multipoles – the interior-type sectoral quadrupole q_{22}^{M} belonging to the mantle and the exterior-type Q_{22}^{IC} belonging to the inner core (Chao, 2017; see below).

The wave-2 deformation observed in GPS (Global Positioning System) should produce corresponding variations in the gravitational field, and the gravitational signature would reside in the [2, 2] component embodied in the spherical-harmonic Stokes coefficients C_{22} and S_{22} of the Earth's external gravitational field. The Stokes coefficients are the (normalized) exterior-type multipoles (Chao and Gross, 1987). In particular, C_{22} and S_{22}, or the external-type sectoral quadrupole, are closely related to the two equatorial moments of inertia, A and B (see below). Therefore in this paper we target the ΔC_{22} and ΔS_{22} (Δ denoting temporal variation referenced to the mean value) obtained from the satellite laser-ranging (SLR) technique and, to a lesser extent, the GRACE satellite, and focus on their temporal amplitude signatures at the 6-year period. The goal is to be able to detect the signals in ΔC_{22} and ΔS_{22} that are expected of the ΔA and ΔB associated with the said deformation in the Earth. Conversely, the quantitative identification of such signals in ΔC_{22} and ΔS_{22} would then corroborate the scenario of the 6-year westward wave-2 motion.

2. Theoretical formulation and predictions

It is customary to express the Earth's external gravitational potential field V in spherical-harmonic expansion referenced to the Earth's mean radius R (Kaula, 1966):

$$V(\mathbf{r}) = \frac{GM}{r}\sum_{n=0}^{\infty}\sum_{m=0}^{n}\left(\frac{R}{r}\right)^{n}\widetilde{P}_{nm}(\cos\theta)(C_{nm}\cos m\lambda + S_{nm}\sin m\lambda) \quad (1)$$

at field point $\mathbf{r}$ = (radius r, co-latitude θ, East longitude λ) in spherical coordinates, where $\widetilde{P}_{nm}(\cos\theta) = (\frac{(2-\delta_{m0})(2n+1)(n-m)!}{(n+m)!})^{\frac{1}{2}} \times$

* Corresponding author.
E-mail address: bfchao@earth.sinica.edu.tw (B.F. Chao).

https://doi.org/10.1016/j.epsl.2020.116316
0012-821X/

$P_{nm}(\cos\theta)$ is the 4π-normalized associated Legendre function; the expansion coefficients C_{nm} and S_{nm} are the $[n,m]$th Stokes coefficients of harmonic degree n order m.

The spherical-harmonic multipole moments (e.g., Jackson, 1962) of mass density distribution $\rho(\mathbf{r})$ of a body, or simply the multipoles here, are defined as the functional inner product (or the "projection") of $\rho(\mathbf{r})$ onto the solid spherical harmonic function integrated over the volume of the body (Backus et al., 1996; Chao, 2017). There are two classes of multipoles corresponding to the two classes of the solid spherical harmonic functions (that satisfy the Laplace equation) – the exterior-type Q-multipoles, which converge for integration radius $r \to 0$, and the interior-type q-multipoles, which converge for integration radius $r \to \infty$:

$$Q_{nm} = \int \rho(\mathbf{r}) r^n Y_{nm}(\Omega) dV;$$
$$q_{nm} = \int \rho(\mathbf{r}) r^{-(n+1)} Y_{nm}(\Omega) dV, \tag{2}$$

where $Y_{nm}(\Omega) = (-1)^m (\frac{(2n+1)(n-m)!}{4\pi(n+m)!})^{\frac{1}{2}} P_{nm}(\cos\theta)\exp(im\lambda)$ (Ω being the solid angle representing θ and λ) is the fully normalized surface spherical harmonic so that $\int Y_{n'm'}(\Omega) Y^*_{nm}(\Omega) d\Omega = \delta_{nn'}\delta_{mm'}$. As such, the Q-multipoles bear heavier weights on the density distribution of the outer layers, and the q-multipoles on the density distribution of the inner layers.

For the Earth, it can be shown (Chao and Gross, 1987) that the (dimensionless) Stokes coefficients are related to the exterior-type Q-multipoles by virtue of Newton's gravitational law, as:

$$C_{nm} + iS_{nm} = \frac{(-1)^m 2\sqrt{(2-\delta_{m0})\pi}}{(2n+1)MR^n} Q_{nm}, \tag{3}$$

where M is the total mass of the Earth. Any (geophysical) mass redistribution in the Earth system in general will give rise to ΔC_{nm} and ΔS_{nm}. Two equivalent (to first order) approaches are applicable to describe an infinitesimal variation: the Eulerian description given by

$$\Delta C_{nm}(t) + i\Delta S_{nm}(t) = \frac{(-1)^m 2\sqrt{(2-\delta_{m0})\pi}}{(2n+1)MR^n} \int \Delta\rho(\mathbf{r};t) r^n Y_{nm}(\Omega) dV, \tag{4}$$

(e.g. Chao et al., 1987), and the Lagrangian description by

$$\Delta C_{nm}(t) + i\Delta S_{nm}(t) = \frac{(-1)^m 2\sqrt{(2-\delta_{m0})\pi}}{(2n+1)MR^n} \int \rho(\mathbf{r};t) r^{n-1} \mathbf{u}(\mathbf{r},t) \cdot \left[n\hat{\mathbf{r}} Y_{nm}(\Omega) + \nabla_1 Y_{nm}(\Omega)\right] dV, \tag{5}$$

(Chao and Gross, 1987), where $\mathbf{u}(\mathbf{r},t)$ is the (3-D) displacement field, and $\nabla_1 = \hat{\boldsymbol{\theta}}\partial_\theta + \csc\theta\hat{\boldsymbol{\lambda}}\partial_\lambda$ is the surface gradient operator.

Focusing on the sectoral $[2,2]$ quadrupoles, we approximate the Earth's gravity by a tri-axial ellipsoid of three near-equal principal moments of inertia $A < B < C$. The corresponding (orthogonal) principal axes are denoted the a, b, c axes, along with the near-equal semi-axes of length in the reverse order.

Since the c axis coincides virtually with the Earth's spin axis or the geographical z axis (the minute departure by the polar motion is $O(10^{-6})$), the a and b axes naturally fall on the equatorial plane. Thus their orientation relative to the geographical x (Greenwich) and y (90°E) axes involves only one single angle of longitude, a configuration that can be treated efficiently by complex notations. The $[2,2]$ Stokes coefficients of a solid body (case in point the Earth or the inner core) are related to the principal moments of inertia A and B via:

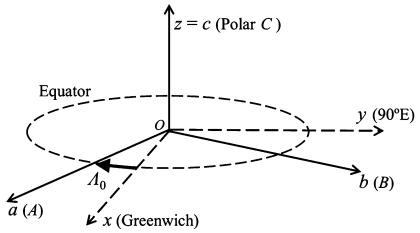

Fig. 1. The three principal axes a, b, c of the Earth (corresponding to the principal moments of inertia $A < B < C$) in the geographical x-y-z coordinates: the c axis points to the North Pole, b points to 75.07°E Longitude, a points to 345.07°E or 14.93°W Longitude or $\Lambda_0 = -14.93°$.

$$C_{22} + iS_{22} = \iiint \rho(x+iy)^2 dV/K = (B-A)\exp(i2\Lambda_0)/K \tag{6}$$

(Liu and Chao, 1991), where $K = 2(5/3)^{1/2}MR^2$ is the normalization factor, and the angle Λ_0 is the East longitude of the equatorial major-axis or the a axis expressed in the geographical coordinates. The complex factor $\exp(i2\Lambda)$ embodies the rotational transformation in the equatorial plane that brings the sectoral quadrupoles from the principal axes (a,b) to the geographical coordinates (x,y). The static $C_{22} = 2.439 \times 10^{-6}$, $S_{22} = -1.400 \times 10^{-6}$ (the Earth gravity model EGM2008 http://icgem.gfz-potsdam.de/tom_longtime), hence Equation (6) gives $B - A = 7.262 \times 10^{-6} MR^2$ and $\Lambda_0 = -14.93°$, i.e. the a axis points to 14.93°W Longitude, and the b axis points to 75.07°E Longitude (towards the Indian Ocean geoid low). The geometry is depicted in Fig. 1. We mention that Equation (6) gives an expression for the changes ΔC_{22} and ΔS_{22} that is independent of the geographical coordinates: $[\Delta C_{22}(t) + i\Delta S_{22}(t)]/[C_{22} + iS_{22}] = [\Delta B(t) - \Delta A(t)]/[B - A] + i2\Delta\Lambda(t)$; the real part is the fractional change of $B - A$, the imaginary part is twice the change in Λ_0 (in radian).

By Equations (2), (3), (6), for $[2,2]$, the external-type multipole $Q_{22} = 5/(8\pi)^{1/2} MR^2 (C_{22} + iS_{22})$ can be expressed as $Q_{22} = |Q_{22}|\exp(i2\Lambda_0)$. The space-time behavior of the westward wave-2 is of the form $\exp[i(\omega t + 2\lambda)]$ with angular frequency $\omega = 2\pi/(6 \text{ years})$. At any given time there are two antipodal westward propagating wave-2 wavefronts, each making only a half-globe or 180° to the opposite longitude in 6 years. Thus, the real full period of each wave-2 wavefront, or the mass transport associated with it (to be treated below), is twice that long, or 12 years at angular frequency $\omega/2$. Yet as far as a point on Earth's surface is concerned, it experiences one full cycle of motion every 6 years. Ding and Chao (2018) have further deduced the phasing or timing of this westward wave-2 propagation from observations. The static orientation of the inner core's equatorial major a axis actually coincides within a few degrees with the Greenwich-Dateline equatorial diameter (a fortuity since the longitude is artificial). The timing of the "initiation" of the westward wave-2 is found (Ding and Chao, 2018) to be the calendar epoch yyyy.mm.dd = 1998.08.09 (and all corresponding cyclic dates of periodicity of 6 years).

By Equations (3), (6) we can now let

$$\Delta C_{22} + i\Delta S_{22} = 2\mu(\xi_a + i\xi_b)^2/K \tag{7}$$

describe the temporal *variation* superposed on the mean static $C_{22} + iS_{22}$ of the whole-Earth gravitational field. Equation (7) follows directly from Equation (6) when expressed in the principal (a,b) coordinates belonging to the inner core, which, as noted above, for all practical purposes coincide with the geographical coordinates (x,y) hence necessitating no extra coordinate rotation of its own. It is parametrized with two parameters: μ is a certain effective mass *anomaly* associated with the peak deformation associated with the propagating wave-2 motion (one μ on each of the two ends of the diametric "dumbbell"). (ξ_a, ξ_b) is the (a,b) component of a certain effective radius ξ of the peak deformation cor-

responding to μ, such that $\xi_a = \xi\cos(\omega t/2)$, $\xi_b = -\xi\sin(\omega t/2)$, or $\xi_a + i\xi_b = \xi\exp(-i\omega t/2)$ tracks the mass transport of the westward wave-2 at the angular frequency $\omega/2$ (see above), with the proper choice of the time origin $t = 0$ which is the afore-mentioned epoch 1998.08.09.

Thus, Equation (7) becomes, in the geographic coordinates:

$$\Delta C_{22}(t) = 2\mu\xi^2\cos\omega t/K, \qquad \Delta S_{22}(t) = -2\mu\xi^2\sin\omega t/K. \quad (8)$$

Equation (8) is what is expected of the time-variations ΔC_{22} and ΔS_{22} in association with the westward wave-2 motion. Specifically one expects: (i) 6-year undulations in both ΔC_{22} and ΔS_{22}; (ii) equal (half-)amplitude of $2\mu\xi^2/K$ for the 6-year ΔC_{22} and ΔS_{22} undulations; (iii) ΔC_{22} peaks at epoch 1998.08.09 (and all other 6-year cyclic dates); (iv) ΔS_{22} leads ΔC_{22} by quarter cycle in phase, or 1.5 years in time, constituting a westward propagation. We shall see in the next section that all these expectations are matched by actual observations.

3. Observational data and analysis

Low-degree Stokes coefficients of the Earth's external gravity field have been measured by the satellite laser-ranging (SLR) techniques for decades (Pearlman et al., 2002). In particular, the temporal variation of the most prominent [2, 0] coefficient, or the oblateness parameter J_2, has been well observed since the late 1970s (e.g., Cheng and Tapley, 2004). The SLR determination of the [2, 2] variations ΔC_{22} and ΔS_{22} (on the order of 10^{-9}) has only become adequately precise since after 1990. In this study we adopt the SLR-derived ΔC_{22} and ΔS_{22} time series (Maier et al., 2012) from the CS22_SLR_AOD.aas dataset (courtesy of the Space Research Institute (IWF) of the Austrian Academy of Sciences). The data are provided at monthly intervals spanning 1992.1–2018.8. In addition to the standard SLR processing (including accounting for the Earth rotation variations), the data have been removed (in accordance with Equation (4)) of the effects of the atmospheric and oceanic mass variations up to degree and order 50, which is developed from general circulation model outputs referenced to Dobslaw et al. (2017) for the GRACE de-aliasing Atmosphere and Ocean De-aliasing (AOD) Level-1B Product Release 06. Two out-lier points (C_{22} of 1993.1 and S_{22} of 1993.2) are interpolated over.

Fig. 2(a, b) presents the ΔC_{22} and ΔS_{22} time series (mean values removed) respectively, along with their wavelet time-frequency spectra. Note the poorer quality (higher noises) of the data during the early few years. Here we apply the real-valued Morlet wavelet so that the temporal undulation of a periodic signal would appear as an alternating phasing of red (peak) and blue (trough) across the timeline (Chao et al., 2014). Fig. 2(c) shows alternatively the absolute value of the wavelet spectrum of the complex $\Delta C_{22} + i\Delta S_{22}$ (brighter shade means stronger signal). Fig. 2(d) gives the conventional discrete Fourier spectrum of $\Delta C_{22} + i\Delta S_{22}$ (for 1992.1–2018.8) where the positive frequency indicates eastward (or prograde) propagation and negative frequency westward (retrograde) propagation. The signal that we shall focus on is the clear, albeit relatively weaker, signal at the ~6-year periodicity in both ΔC_{22} (Fig. 2a) and ΔS_{22} (Fig. 2b) as well as in the retrograde $\Delta C_{22} + i\Delta S_{22}$ (in Figs. 2c, 2d).

Some other periodic or quasi-period signals are also evident in the spectra. They include notably the remnant annual and semi-annual signals resulting presumably from the seasonality in the atmospheric and hydrospheric mass redistribution unaccounted for by the AOD model correction, a ~2-year turning into ~3-year signal in the wavelet spectra whose origin is presently unidentified, and some slow undulation masquerading as a nominal ~31-year periodicity in the Fourier spectrum.

To extract the 6-year signal, we take the temporal undulation profiles across the wavelet spectra (i.e. along the horizontal timeline of Figs. 2a, b) at that periodicity, which are shown in Fig. 3 (the solid curves). The amplitude of the undulation is calibrated, hence rendered true, after scaled with respect to the wavelet of a synthetic 6-year sinusoid of unity amplitude. They are overlaid with the synthetic simulated 6-year ΔC_{22} and ΔS_{22} (dotted curves), what is expected of Equation (8) with the expected timing or phasing for both, while the amplitude ($2\mu\xi^2/K$) is to match those of the observed ΔC_{22} and ΔS_{22} in least-squares fits. The comparison complies remarkably well with the expectations (i) though (iv) raised in Section 2 – their (nearly) equal amplitudes, the quarter-cycle phase lead of ΔS_{22} relative to ΔC_{22}, and the matching of their timing with respect to the epoch 1998.08.09, are all well asserted.

We have also tested the case using the IWF SLR dataset without the AOD correction. The results (presented in the Supplement Figures S1 and S2) only differ insignificantly as far as the 6-year signal is concerned, with ΔC_{22} in fact matching even a bit closer to the expectation.

The GRACE (Gravity Recovery And Climate Experiment; Tapley et al., 2004) satellite mission also provided time-variable gravity data during its lifetime 2002-2017, including ΔC_{22} and ΔS_{22}. For comparison, we inspect the GRACE data series from the Center for Space Research RL06 solutions. The results are given in the Supplement Figures S3 and S4, which show nearly the same but somewhat poorer matches than the SLR's during GRACE's shorter timespan. This is attributed to the recognized fact that the GRACE's low-degree Stokes coefficients (especially degree-2) are relatively poorly determined in comparison with SLR (Cheng et al., 2011).

What remains to be vindicated is for the estimated amplitude $2\mu\xi^2/K$ for ΔC_{22} and ΔS_{22} to match the wave-2 displacement observed by GPS in Ding and Chao (2018). We do so via Equation (5), with the associated Legendre function $P_{22} = 3\sin^2\theta$, where we neglect the horizontal components as their contributions are several times smaller than the vertical. To estimate the maximum (half-)amplitude of the vertical displacement of the form [2, 2], we substitute $\mathbf{u} = \hat{\mathbf{r}}U(r)Y_{22}^*(\Omega)$ into Equation (5), and get approximately $(\sqrt{2\pi}/10)[\rho U]_{\rm um}R^2/M$ for the right-side of Equation (5), where $[\rho U]_{\rm um}$ indicates that of the upper mantle considering the fact that the integral in Equation (5) is weighted heavily towards outer parts of the Earth (as r^3). Substituting in the following numerical values: the upper-mantle $\rho_{\rm um} \sim 4000$ kg/m^3, the Y_{22}'s maximum value of $\sqrt{15/(2\pi)}/4 = 0.386$, and the (half-)amplitude of the observed 6-year $|\Delta C_{22} + i\Delta S_{22}| \sim 2\times10^{-11}$ (see Fig. 3), we get the (half-)amplitude of the upper-mantle $u \approx 5\sqrt{15}M|\Delta C_{22} + i\Delta S_{22}|/(4\pi[\rho]_{\rm um}R^2) \sim 1.1$ mm. This rough estimate agrees well with the observed surface displacement from Ding and Chao (2018) as follows: The latter reported the surface vertical U of 4.3 mm, which amounts to a peak $u = 4.3$ mm $\times$ $0.386 = 1.6$ mm. We note that there is no a priori reason for these two independently observed values, if un-related, to match to the extent they do. A more refined determination would entail realistic modeling of the mantle's layered rheology, which is beyond our present scope.

4. Discussion and conclusions

Previous study (Ding and Chao, 2018) of a westward-propagating wave-2 displacement field in the mantle predicts a retrograde variation of the [2, 2] sectoral quadrupole or the Earth's gravitational Stokes coefficients C_{22} and S_{22}, which in turn signifies a corresponding variation in the Earth's two equatorial principle moments of inertia. In this paper we search such predicted 6-year variations in ΔC_{22} and ΔS_{22} monthly data series that have been available from SLR since early 1990s now spanning over 4

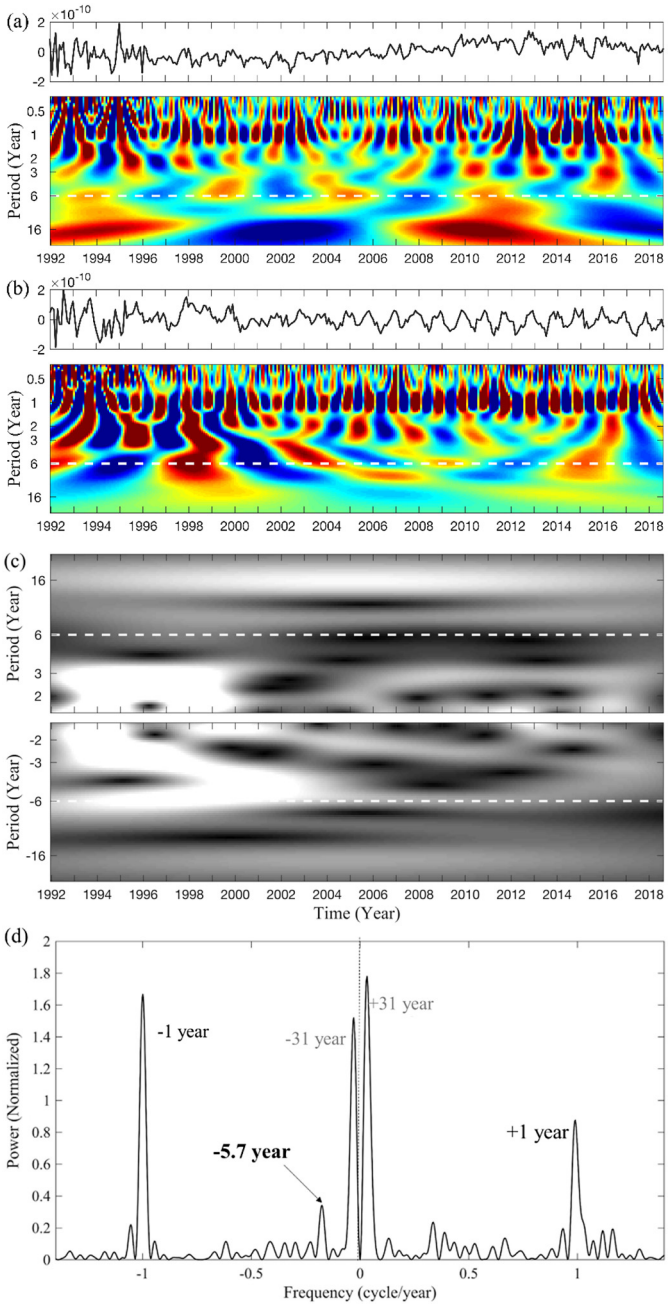

Fig. 2. (a) ΔC_{22} time series (mean value removed), 1992-2018, along with its (real-valued Morlet) wavelet time-frequency spectra (red means peak value and blue trough value). (b) The same as (a) but for ΔS_{22}. (c) The absolute value of the wavelet spectrum of the complex $\Delta C_{22} + i\Delta S_{22}$ (brighter shade means stronger signal). (d) The conventional Fourier spectrum of $\Delta C_{22} + i\Delta S_{22}$ (positive frequency indicates the eastward (or prograde) propagation and negative frequency the westward (retrograde) propagation). Note the (retrograde) ~6-year periodicity in all spectra (−5.7-year in (d)). (For interpretation of the colors in the figure(s), the reader is referred to the web version of this article.)

cycles. We find unequivocal evidences for their existence, which well match the predictions in terms of relative amplitude and relative phasing, as well as the absolute calendar dates. The matching is also good in the absolute amplitude of the required upper-mantle vertical peak displacement (~1.1 mm) with that of the GPS-observed surface displacement (~1.6 mm) in want of detailed modeling.

There are of course other (broad-band) mass transports going on in the Earth system that contain [2, 2] energy (hence present themselves in ΔC_{22} and ΔS_{22}) at ~6-year timescale but are unrelated to our targeted wave-2 motion. Besides the measurement errors, they are the main sources of geophysical "contaminations" to our numerical processing of ΔC_{22} and ΔS_{22}, seen as the (moderate) mismatches in Figs. 2 and 3. Presumably the largest likely geophysical contamination comes from the interannual mass transports in the water cycles in the atmosphere + ocean + land hydrology, but note that a modeled atmospheric + oceanic mass transports had been removed beforehand in the form of AOD model correction (using Equation (2)) from the IWF SLR data series that we utilize.

The datasets we analyze are single time series of ΔC_{22} and ΔS_{22} pertaining to the Earth as a whole, in contrast to the point measurements from global arrays of GPS or geomagnetism for which the data stacking can effectively isolate the target signals as done in Ding and Chao (2018). Given the fact that the signal-to-noise ratio of the 6-year signals in ΔC_{22} and ΔS_{22} is not high,

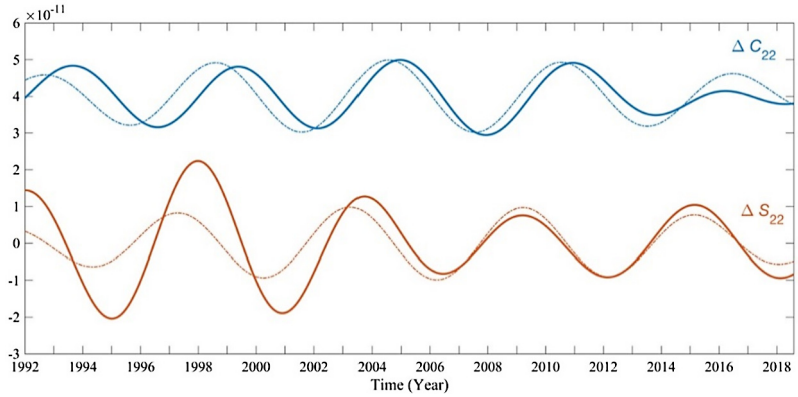

Fig. 3. The (calibrated) temporal undulation of ΔC_{22} and ΔS_{22} (profiling across the wavelet spectra in Fig. 2a, b) at the 6-year periodicity (solid curves); overlaid with the synthetic simulated 6-year ΔC_{22} and ΔS_{22} (dotted curves) expected of the westward wave-2 motion with least-squares matched amplitudes.

our detection of the 6-year signals is based on the time-frequency wavelet spectrum, whilst the Fourier power spectra can marginally resolve them. This in fact attests to the efficacy of the wavelet spectrum in detecting and analyzing weak (quasi-)periodic signals.

Declaration of competing interest

The authors declare that they have no known competing financial interests or personal relationships that could have appeared to influence the work reported in this paper.

Acknowledgements

The SLR Stokes coefficient data are provided by the Space Research Institute (IWF) of the Austrian Academy of Sciences via website http://geodesy.iwf.oeaw.ac.at/d_slr_monthly.html, based on SLR observations coordinated by ILRS (https://ilrs.cddis.eosdis.nasa.gov/). The GRACE satellite data are available by ftp://podaac-ftp.jpl.nasa.gov/allData/grace/L2/CSR/RL06. We thank Hao Ding for discussion and Yuwen Li for assistance in data preparation. This work is supported by Taiwan Ministry of Science and Technology via grants #106-2116-M-001-013 and #108-2116-M-001-016.

Appendix A. Supplementary material

Supplementary material related to this article can be found online at https://doi.org/10.1016/j.epsl.2020.116316.

References

Backus, G., Parker, R., Constable, C., 1996. Foundations of Geomagnetism. Cambridge Univ. Press, New York.

Chao, B.F., 2017. Dynamics of axial torsional libration under the mantle-inner core gravitational interaction. J. Geophys. Res. 121. https://doi.org/10.1002/2016JB013515.

Chao, B.F., Gross, R.S., 1987. Changes in the Earth's rotation and low-degree gravitational field induced by earthquakes. Geophys. J. R. Astron. Soc. 91, 569–596.

Chao, B.F., O'Connor, W.P., Chang, A.T.C., Hall, D.K., Foster, J.L., 1987. Snow-load effect on the Earth's rotation and gravitational field, 1979-1985. J. Geophys. Res. 92, 9415–9422.

Chao, B.F., Chung, W.Y., Shih, Z.R., Hsieh, Y.K., 2014. Earth's rotation variations: a wavelet analysis. Terra Nova 26, 260–264. https://doi.org/10.1111/ter.12094.

Cheng, M., Ries, J.C., Tapley, B.D., 2011. Variations of the Earth's figure axis from satellite laser ranging and GRACE. J. Geophys. Res. 116, B01409. https://doi.org/10.1029/2010JB000850.

Cheng, M.K., Tapley, B.D., 2004. Variations in the Earth's oblateness during the past 28 years. J. Geophys. Res. 109. https://doi.org/10.1029/2004JB003028.

Ding, H., Chao, B.F., 2018. A 6-year westward rotary motion in the Earth: detection and possible MICG coupling mechanism. Earth Planet. Sci. Lett. 495, 50–55. https://doi.org/10.1016/j.epsl.2018.05.009.

Dobslaw, H., Bergmann-Wolf, I., Dill, R., Poropat, L., Thomas, M., Dahle, C., Esselborn, S., Konig, R., Flechtner, F., 2017. A new high-resolution model of non-tidal atmosphere and ocean mass variability for de-aliasing of satellite gravity observations: AOD1B RL06. Geophys. J. Int. 211, 263–269.

Jackson, J.D., 1962. Classical Electrodynamics. John Wiley and Sons, New York.

Kaula, W.M., 1966. Theory of Satellite Geodesy. Blaisdell, Waltham, MA.

Liu, H.S., Chao, B.F., 1991. The Earth's equatorial principal axes and moments of inertia. Geophys. J. Int. 106, 699–702.

Maier, A., Krauss, S., Hausleitner, W., Baur, O., 2012. Contribution of satellite laser ranging to combined gravity field models. Adv. Space Res. 49 (3), 556–565. https://doi.org/10.1016/j.asr.2011.10.026.

Pearlman, M.R., Degnan, J.J., Bosworth, J.M., 2002. The international laser ranging service. Adv. Space Res. 30, 135–143. https://doi.org/10.1016/S0273-1177(02)00277-6.

Tapley, B.D., Bettadpur, S., Watkins, M., Reigber, C., 2004. The gravity recovery and climate experiment: mission overview and early results. Geophys. Res. Lett. 31, L09607. https://doi.org/10.1029/2004GL019920.